Journal of Energy Chemistry 84 (2023) 153–161

Contents lists available at ScienceDirect

Journal of Energy Chemistry

journal homepage: www.elsevier.com/locate/jechem

http://www.journals.elsevier.com/journal-of-energy-chemistry/

Occurrence of anionic redox with absence of full oxidation to Ru^{5+} in high-energy P2-type layered oxide cathode

Jinho Ahn [a,b,1], Hyunyoung Park [a,b,1], Wonseok Ko [a,b], Yongseok Lee [a,b], Jungmin Kang [a,b], Seokjin Lee [a,b], Sangyeop Lee [a,b], Eunji Sim [c,d], Kyuwook Ihm [c], Jihyun Hong [e], Jung-Keun Yoo [f], Kyojin Ku [g,*], Jongsoon Kim [a,b,*]

[a] Department of Energy Science, Sungkyunkwan University, Suwon 16419, Republic of Korea
[b] SKKU Institute of Energy Science and Technology (SIEST), Sungkyunkwan University, Suwon 16419, Republic of Korea
[c] Nano & Interface Research Team, Pohang Accelerator Laboratory, Pohang 37673, Republic of Korea
[d] Department of Smart Fabrication Technology, Sungkyunkwan University, Suwon 16419, Republic of Korea
[e] Energy Materials Research Center, Korea Institute of Science and Technology (KIST), 14 Gil 5 Hwarang-ro, Seongbuk-gu, Seoul 02792, Republic of Korea
[f] Carbon Composites Department, Composites Research Division, Korea Institute of Materials Science (KIMS), 797 Changwondaero, Changwon 51508, Republic of Korea
[g] Department of Materials Science and Engineering, Hanbat National University, Daejeon 34158, Republic of Korea

ARTICLE INFO

Article history:
Received 13 March 2023
Revised 20 April 2023
Accepted 16 May 2023
Available online 26 May 2023

Keywords:
Na-ion batteries
P2-type cathode
Anionic redox
Local environment
First-principles calculation

ABSTRACT

The anionic redox has been widely studied in layered-oxide-cathodes in attempts to achieve high-energy-density for Na-ion batteries (NIBs). It is known that an oxidation state of Mn^{4+} or Ru^{5+} is essential for the anionic reaction of O^{2-}/O^{-} to occur during Na^+ de/intercalation. However, here, we report that the anionic redox can occur in Ru-based layered-oxide-cathodes before full oxidation of Ru^{4+}/Ru^{5+}. Combining studies using first-principles calculation and experimental techniques reveals that further Na^+ deintercalation from P2-$Na_{0.33}[Mg_{0.33}Ru_{0.67}]O_2$ is based on anionic oxidation after 0.33 mol Na^+ deintercalation from P2-$Na_{0.67}[Mg_{0.33}Ru_{0.67}]O_2$ with cationic oxidation of $Ru^{4+}/Ru^{4.5+}$. Especially, it is revealed that the only oxygen neighboring 2Mg/1Ru can participate in the anionic redox during Na^+ de/intercalation, which implies that the Na–O–Mg arrangement in the P2-$Na_{0.33}[Mg_{0.33}Ru_{0.67}]O_2$ structure can dramatically lower the thermodynamic stability of the anionic redox than that of cationic redox. Through the O anionic and Ru cationic reaction, P2-$Na_{0.67}[Mg_{0.33}Ru_{0.67}]O_2$ exhibits not only a large specific capacity of ~172 mA h g^{-1} but also excellent power-capability via facile Na^+ diffusion and reversible structural change during charge/discharge. These findings suggest a novel strategy that can increase the activity of anionic redox by modulating the local environment around oxygen to develop high-energy-density cathode materials for NIBs.

1. Introduction

Environmental issues including climate change, air pollution, and the greenhouse effect have accelerated the change of the energy paradigm from fossil fuels to eco-friendly renewable energy [1–3]. In this respect, Li-ion batteries (LIBs) have received great attention as an efficient energy storage system with high energy density and long cycle life [4,5]. However, the cost issues stemming from the limited and concentrated sources of Li on Earth are considered the main problems preventing grid-scale application of LIBs [6,7]. Recently, Na-ion batteries (NIBs) based on unlimited Na sources have been widely studied as an attractive alternative to LIBs as large-scale energy storage systems [8–11]. Thus, many researchers have focused on the development of novel cathode materials for NIBs.

Among various cathode materials, the layered-type oxide has received great attention as a promising cathode for NIBs. They consist of repeating edge-shared transition metal oxide (MO_6) layers and alkali metal layers along the *c*-axis, represented by the P2 and O3 structures, respectively. Due to their dense packing structure with facile ionic diffusion through 2-dimensional diffusion

* Corresponding authors.
E-mail addresses: kjku@hanbat.ac.kr (K. Ku), jongsoonkim@skku.edu (J. Kim).

[1] These authors contributed equally to this work.

https://doi.org/10.1016/j.jechem.2023.05.016

pathway, these materials exhibit higher electrochemical properties than other cathode materials, resulting in a large gravimetric energy density and high rate-capability. Moreover, several layered-type cathodes can exhibit not only transition-metal (TM)-based cationic redox reaction but also oxygen-based anionic redox reaction during charge/discharge, resulting in a large available capacity and energy density [12–14].

Recent studies have shown intensive interest in investigating anionic redox reactions in layered-type cathodes due to their potential to significantly improve the energy density of NIBs. Thus, to prepare the anionic-redox-based layered-type cathodes, the oxidation states of TM cations such as Mn and Ru in the pristine state were controlled toward high values such as Mn^{4+} or Ru^{5+} through substitution of TM cations with low valence state of X element, such as Li^+, Mg^{2+}, Zn^{2+}, etc. [15–17]. According to previous research, the oxygen-redox reaction is induced when a linear Na-O-X configuration is formed, which results in the formation of unhybridized O 2*p* non-bonding orbitals. These orbitals have higher energy levels than other hybridized O 2*p* orbitals, allowing them to donate electrons before the TM t_{2g} orbitals. This phenomenon can be achieved with selection of appropriate TM elements, such as Mn^{4+} and Ru^{5+}, which have t_{2g} orbitals located at a lower energy level than the O 2*p* non-bonding orbital [18,19]. In particular, the 4*d* transition metal Ru element is known to exhibit a strong covalent bond with oxygen, which effectively stabilizes oxidized oxygen species and leads to reversible anionic redox reactions [20,21]. Therefore, comprehending the influence of the local environment (both of Ru and O) on the anionic redox reactions is necessary.

In this study, we reported that the anionic redox reaction in a Ru-based layered-type oxide was influenced by the local environment to the neighboring oxygen anions rather than the oxidation state of the Ru cation. Through combining studies using first-principles calculation and experimental techniques, we revealed that the oxygen anionic redox reaction can occur before the all Ru^{4+} cations in P2-type $Na^+_{0.67}[Mg^{2+}_{0.33}Ru^{4+}_{0.67}]O^{2-}_2$ (P2-NMRO) are oxidized to Ru^{5+}. Ru^{4+}/Ru^{5+} cationic redox reaction only compensates 0.33 mol Na^+ deintercalation with a gradual increase in the operation voltage. Unexpectedly, further Na^+ deintercalation from P2-$Na_{0.33}[Mg_{0.33}Ru^{4.5+}_{0.67}]O_2$ results in the oxidation of oxygen anions instead of Ru cations, inducing an abrupt increase in the operation voltage. The first-principles calculation results revealed the oxygen anions neighboring 2 Mg and 1 Ru cations provide labile electrons that can participate in the anionic redox reactions, unlike the other oxygen anions in the P2-NMRO structure. Through cationic redox of the Ru cation and anionic redox of the O anion, a total of ~0.8 mol Na^+ was reversibly de/intercalated from/into the P2-NMRO structure at a current density of 10.9 mA g^{-1}, corresponding to a large specific capacity of ~172 mA h g^{-1}. Even at 1090 mA g^{-1}, up to ~76% of the specific capacity of P2-NMRO at 10.9 mA g^{-1} was retained, indicating the outstanding power-capability by facile Na^+ diffusion during the cationic and anionic redox reactions.

2. Experimental

2.1. Material preparation

P2-$Na_{0.67}[Mg_{0.33}Ru_{0.67}]O_2$ was synthesized using a simple solid-state method. Appropriate amounts of Na_2CO_3 (99.5%, Sigma Aldrich), MgO (99.9%, Alfa Aesar), and RuO_2 (99%, Alfa Aesar) were homogenously mixed using high-energy planetary ball-milling at 500 r min^{-1} for 12 h. The mixed powder was pelletized and calcined at 1000 °C for 18 h under air gas flow.

2.2. Material characterization

X-ray diffraction (XRD) was performed using PANalytical Empyrean with Cu K_α radiation (λ = 1.54 Å). The 2θ range was 10°–80° with a step size of 0.026°. Rietveld refinement was performed using FullProf software [22]. Operando XRD was performed during initial charge/discharge at a current density of 15 mA g^{-1} in the voltage range of 1.5–4.4 V (vs. Na^+/Na). The operando synchrotron XRD patterns were obtained at the 3D XRS beamline at the Pohang Accelerator Laboratory (PAL), South Korea, using synchrotron radiation (λ = 0.688438 Å) with a Mar345 image detector. The 2θ angles of collected operando synchrotron XRD patterns were converted to angles corresponding to λ = 1.54178 Å (the wavelength of a conventional X-ray tube source with Cu K_α) for easy comparison with other studies.

The morphology of the synthesized particles was observed using field-emission scanning electron microscopy (FE-SEM: JSM-7600, JEOL Ltd.) operated at 15 keV. A Pt coating was applied to improve the conductivity of the measured samples.

High-resolution transmission electron microscopy (HR-TEM) images, *d*-space with selected area electron diffraction (SAED) patterns, and energy-dispersive X-ray spectroscopy (EDS) elemental mapping images were obtained using field-emission transmission electron microscopy (FE-TEM; JEM-F200, JEOL Ltd.) at the National Center for Inter-University Research Facilities (NCIRF) at Seoul National University.

Ru K-edge X-ray absorption spectroscopy (XAS) spectra were obtained at beamline 7D XAFS at PAL. The spectra were collected in transmission mode, and Ru reference data were simultaneously measured from Ru metal foil. O K-edge soft X-ray absorption spectroscopy (sXAS) spectra were obtained in total fluorescence yield (TFY) mode with a photon energy range of 525–565 eV at beamline 4D PES at PAL. All of the measured data were analyzed using Athena software [23].

X-ray photoelectron spectroscopy (XPS) analysis was performed using an AXIS SUPRA (Kratos, USA) at the National Center for Inter-University Research Facilities (NCIRF) at Seoul National University.

2.3. Electrochemical characterization

The P2-$Na_{0.67}[Mg_{0.33}Ru_{0.67}]O_2$ electrode was fabricated by mixing 80 wt% of the active material, 10 wt% of Super P carbon black, and 10 wt% of polyvinylidene fluoride (PVDF) using *N*-methyl-2-pyrolidone (NMP) as the solvent. The slurry was cast on Al foil and dried at 100 °C overnight under vacuum. After drying, the electrode was punched into disks of 10π-mm diameter. In addition, the mass loading of the electrode was ~2 mg cm^{-2}. R2032-type coin cells were assembled as half-cells using Na metal as the counter electrode, a separator (Whatman GF/F glass fiber), and 1 M $NaPF_6$ in propylene carbonate (PC): fluoroethylene carbonate (FEC) = 98:2 (*v*/*v*) as the electrolyte. The coin cells were assembled in an Ar-filled glove box. Galvanostatic charge/discharge tests were performed at various current densities (10.9, 21.8, 43.6, 109, 218, 436, and 1090 mA g^{-1} in the voltage range of 1.5–4.4 V (vs. Na^+/Na); the charge current density was fixed at 10.9 mA g^{-1}) using an automatic battery charge/discharge test system (WBCS 3000, WonATech).

2.4. Computational details

All the density functional theory (DFT) calculations were performed using the Vienna Ab initio Simulation Package (VASP) [24]. Projector-augmented wave pseudopotentials were used with a plane-wave basis set, as implemented in VASP [25]. Perdew-Burke-Ernzerhof (PBE) parametrization of the generalized gradient approximation (GGA) [26] was used for the exchange–correlation

functional. For the DFT calculations, a 6 × 3 × 3 *k*-point grid was used to calculate a 2 × 3 × 1 supercell structure of P2-NMRO. The GGA+U method [27] was adopted to address the localization of the *d*-orbital in Ru ions, with a *U* value of 4.0 eV, as used in previous studies [28,29]. A kinetic energy cutoff of 500 eV was used in all the calculations, and all the structures were optimized until the force in the unit cell converged to within 0.03 eV $Å^{-1}$. Cluster-assisted statistical mechanics (CASM) [30] was used to generate all the Na^+/vacancy configurations for each composition, followed by full DFT calculations on a maximum of 20 configurations with the lowest electrostatic energy for each composition used to obtain the convex hull plot of P2-NMRO. The nudged elastic band (NEB) calculations [31] were performed to determine the activation barrier for Na^+ diffusion in the P2-NMRO structure. To perform the calculations, five intermediate images were generated between each Na site. These structures were then calculated using the NEB algorithm with fixed lattice parameters and free internal atomic positions. The schematic illustrations, crystal structure, and NEB calculation results for Na^+ diffusion pathways were drawn using VESTA software [32].

3. Results and discussion

3.1. Preparation and structural characterization of P2-$Na_{0.67}[Mg_{0.33}Ru_{0.67}]O_2$

We synthesized the P2-NMRO, as illustrated in Fig. 1(a). It consisted of the ABBA stacking sequence of the oxygen layer, in which the metal and Na ions occupied octahedral and prismatic-type (P-type) sites, respectively. Rietveld refinement on the XRD pattern indicates that P2-NMRO has a hexagonal crystal structure with $P6_3/mmc$ space group and P2-type layered stacking (Fig. 1b). The lattice parameters of P2-NMRO were calculated to be: $a = b = 2.9573(7)$ Å and $c = 11.2423(3)$ Å. The detailed structural information of P2-NMRO such as the Wyckoff positions, B_{iso}, and occupancy is presented in Table S1. The morphology and chemical composition were confirmed using TEM and EDS elemental mapping. Fig. 1(c) shows the particle with a size of ~1 μm and homogeneously distributed Na, Mg, and Ru elements. The elemental ratio of Na:Mg:Ru in P2-NMRO was determined to be 0.67:0.33:0.67 from EDS, which is consistent with the SEM and inductively coupled plasma atomic emission spectroscopy (ICP-AES) results (Fig. S1 and Table S2). Moreover, SAED analysis revealed that NMRO consisted of a single-crystalline particle of well-defined P2-type layered structure with (102), (104), and (106) planes along the [020] zone axis (Fig. 1d).

3.2. Electrochemical behavior and structural change of P2-$Na_{0.67}[Mg_{0.33}Ru_{0.67}]O_2$

P2-NMRO delivered high discharge capacity with outstanding power-capability (Fig. 2a and b). Although it exhibited a discharge capacity of 172 mA h g^{-1} at 10.9 mA g^{-1}, 130 mA h g^{-1} of the capacity was obtained at 1090 mA g^{-1}, corresponding to 76% of the capacity at 10.9 mA g^{-1}. To investigate the origin of the high power-capability, we predicted the theoretical Na^+ diffusion pathway in the P2-NMRO structure using the NEB method based on first-principles calculation, as shown in Fig. 2(c and d) [31]. Attributed to the two-dimensional pathway along the large slab-space in P-type layered oxides, the low diffusion barrier at 137.4 meV enables facile Na^+ diffusion in the structure. In addition, P2-NMRO delivers a capacity retention of ~72% for 100 cycles at a current density of 218 mA g^{-1} with high coulombic efficiency of over 99% (Fig. S2).

The theoretical electrochemical behavior of P2-NMRO was further investigated using first-principles calculations. We calculated the formation energy for numerous Na^+/vacancy configurations in the $Na_x[Mg_{0.33}Ru_{0.67}]O_2$ ($0 \le x \le 1$) structure during Na^+ de/intercalation. The theoretical redox potentials were determined using formation energy results and the following equation.

$$V = -\frac{E[Na_{x_2}Mg_{0.33}Ru_{0.67}O_2] - E[Na_{x_1}Mg_{0.33}Ru_{0.67}O_2] - (x_2 - x_1)E[Na]}{(x_2 - x_1)F}$$

In the above equation, V is the average redox potential as a function of Na content in the range of $x_1 \le x \le x_2$; E is the calculated formation energy of the most stable state for each

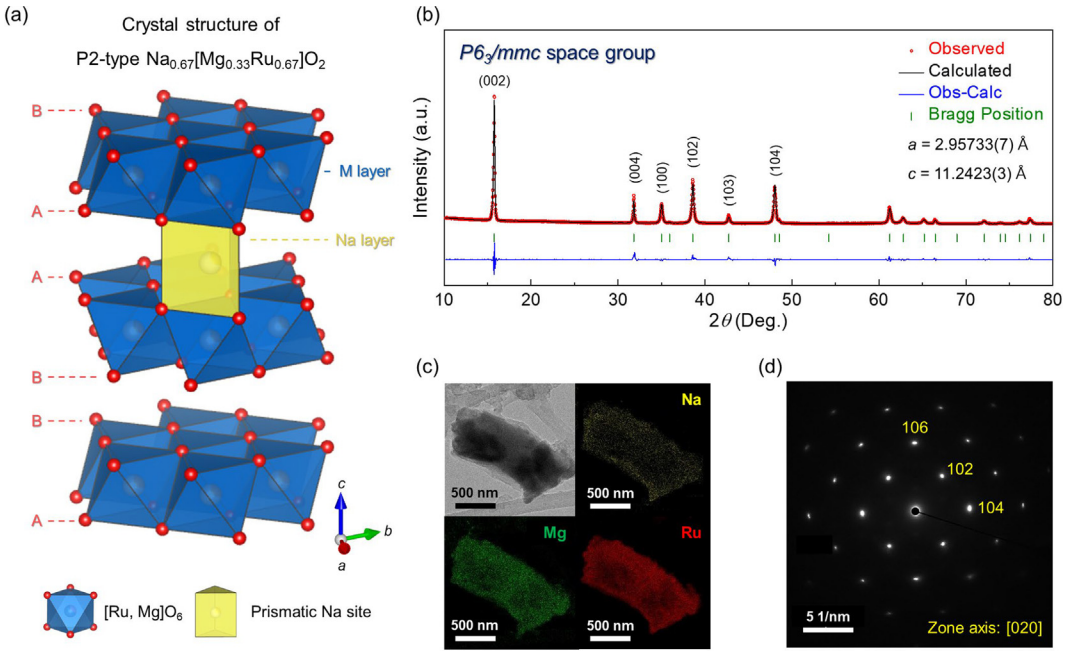

Fig. 1. (a) Crystal structure of P2-type $Na_{0.67}[Mg_{0.33}Ru_{0.67}]O_2$. (b) XRD pattern and Rietveld refinement results of P2-$Na_{0.67}[Mg_{0.33}Ru_{0.67}]O_2$ (R_p = 12.8%, R_{wp} = 13.7%, χ^2 = 8.16). (c) TEM-EDS mapping results (atomic ratio of Na:Mg:Ru = 2.05:1:2.02). (d) SAED pattern along [020] zone axis.

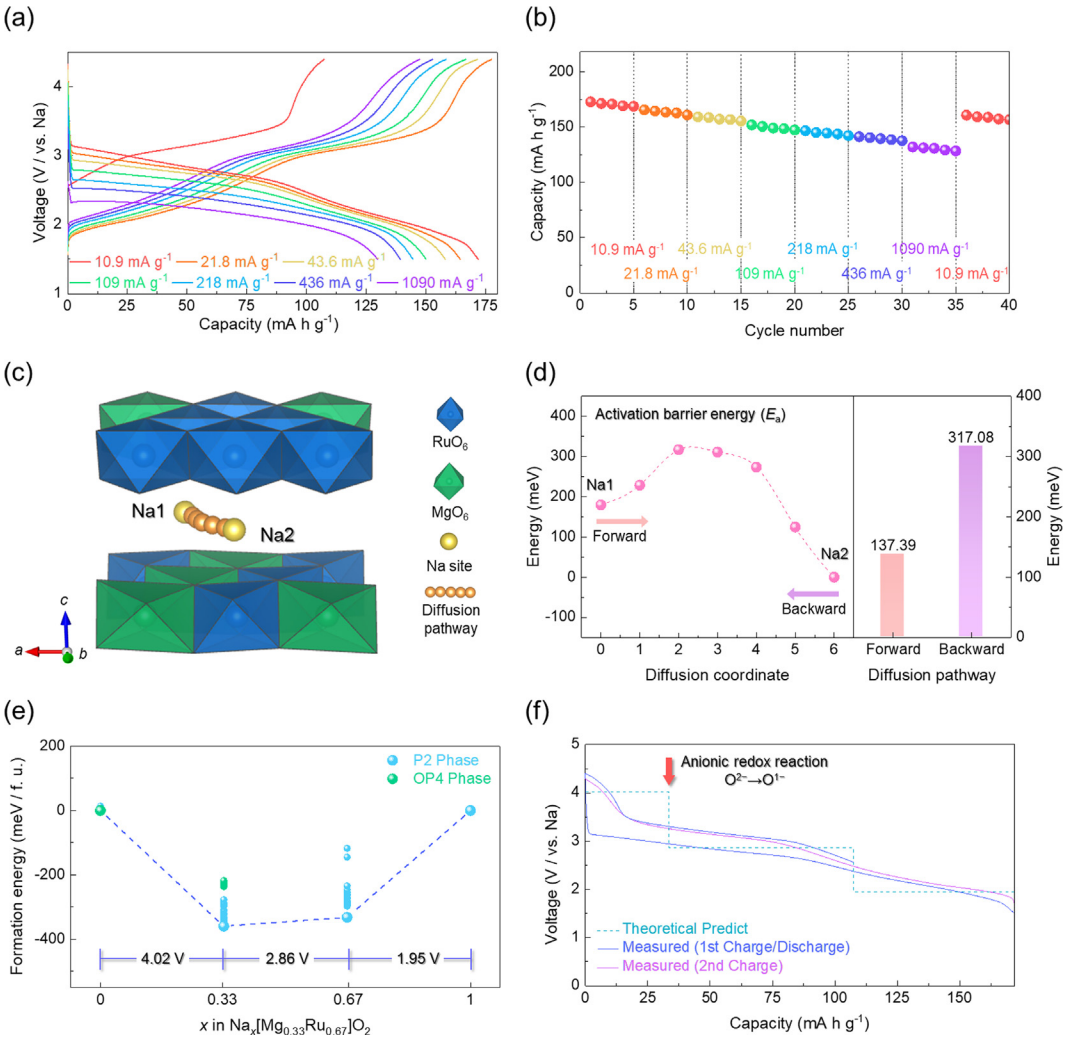

Fig. 2. (a) Charge/discharge curves of P2-$Na_{0.67}[Mg_{0.33}Ru_{0.67}]O_2$ in the voltage range of 1.5–4.4 V at various discharge current densities and a charge current density of 10.9 mA g^{-1}. (b) Rate-capability of P2-$Na_{0.67}[Mg_{0.33}Ru_{0.67}]O_2$. (c) Predicted Na^+ diffusion pathway in P2-$Na_{0.67}[Mg_{0.33}Ru_{0.67}]O_2$ and (d) predicted activation barrier energy for Na^+ diffusion in P2-$Na_{0.67}[Mg_{0.33}Ru_{0.67}]O_2$. (e) Formation energy of P2-$Na_x[Mg_{0.33}Ru_{0.67}]O_2$ ($0 \le x \le 1$) determined using convex-hull method. (f) Comparison of theoretical voltage prediction and charge/discharge profiles for $Na_x[Mg_{0.33}Ru_{0.67}]O_2$.

$Na_x[Mg_{0.33}Ru_{0.67}]O_2$ ($0 \le x \le 1$) composition; E[Na] represents the Na metal energy; and F is the Faraday constant. These formation energies were compared and arranged using a convex-hull plot, and the thermodynamically stable crystal structure of $Na_x[Mg_{0.33}Ru_{0.67}]O_2$ was confirmed (Fig. 2e). The predicted redox potentials are also consistent with electrochemically measured 1st charge/discharge profiles of P2-NMRO in the voltage range of 1.5–4.4 V at a current density of 10.9 mA g^{-1} (Fig. 2f), where P2-NMRO delivered charge/discharge capacities of 107 and 172 mA h g^{-1} corresponding to 0.49 and 0.79 mol Na^+ de/intercalation, respectively.

Moreover, one of the important points on the DFT calculation results is more stable OP4 phase than P2 phase after full Na deintercalation from $Na_x[Mg_{0.33}Ru_{0.67}]O_2$, indicating the occurrence of a P2/OP4 phase transition at low Na contents. Interestingly, the structural analyses during the initial cycle demonstrate that P2-NMRO exhibits unclearly distinct two-phase reaction like other P2-type cathode materials but the continuous phase reaction of P2-OP4 transition, which can contribute to the stable electrochemical performance of P2-NMRO. Operando XRD data in the voltage range of 1.5–4.4 V at a current density of 15 mA g^{-1} are presented in Fig. 3(a). The position and intensity of the XRD peaks corresponding to the (0 0 2) and (1 0 0) planes monotonously changed during charge and discharge (Fig. 3b and c). During the initial part of charging, the (0 0 2) peak shifted toward lower angle by the repulsive interaction between O^{2-} ions after partial Na^+ extraction. With further desodiation, the continuous phase reaction of the P2-OP4 transition was observed in P2-NMRO unlike other P2 materials that exhibited the P2-O2 phase transition, which is more detrimental to the electrochemical performance [33,34]. Also, operando XRD data clearly indicate that distorted P'2 phase was detected during discharge. At the pristine state, P2-NMRO contains 0.67 mol Na^+ in its structure, and undergoes the redox reaction in which 0.49 mol Na^+ are deintercalated upon full charging to 4.4 V and 0.79 mol Na^+ are intercalated upon full discharging to 1.5 V. Therefore, more reduced Ru cations in the 1.5 V-discharged sample than those in the pristine sample result in the changes of the *a*- and *c*-lattice parameters due to the enlargement of the ionic size of Ru. In this process, slight distortion of the RuO_6 octahedral leads to the phase transition from P2 to P'2. As shown in Fig. S3, formation of the distorted P'2 phase during discharge was confirmed through the comparison of the XRD patterns between the pristine and the 1.5 V-discharged samples. In addition, according to the Rietveld refinement of operando XRD data (Fig. S4), the lattice parameters *c* and *a* decreased from 11.3 to 10.7 Å and from 2.96 to 2.90 Å, respectively, during charging process. After that, they were reversibly recovered back to the original structure upon discharge (Fig. 3d and e). The total *c*/*a* ratio change of P2-NMRO was only ~4%, indicating a small degree of anisotropic lattice change during

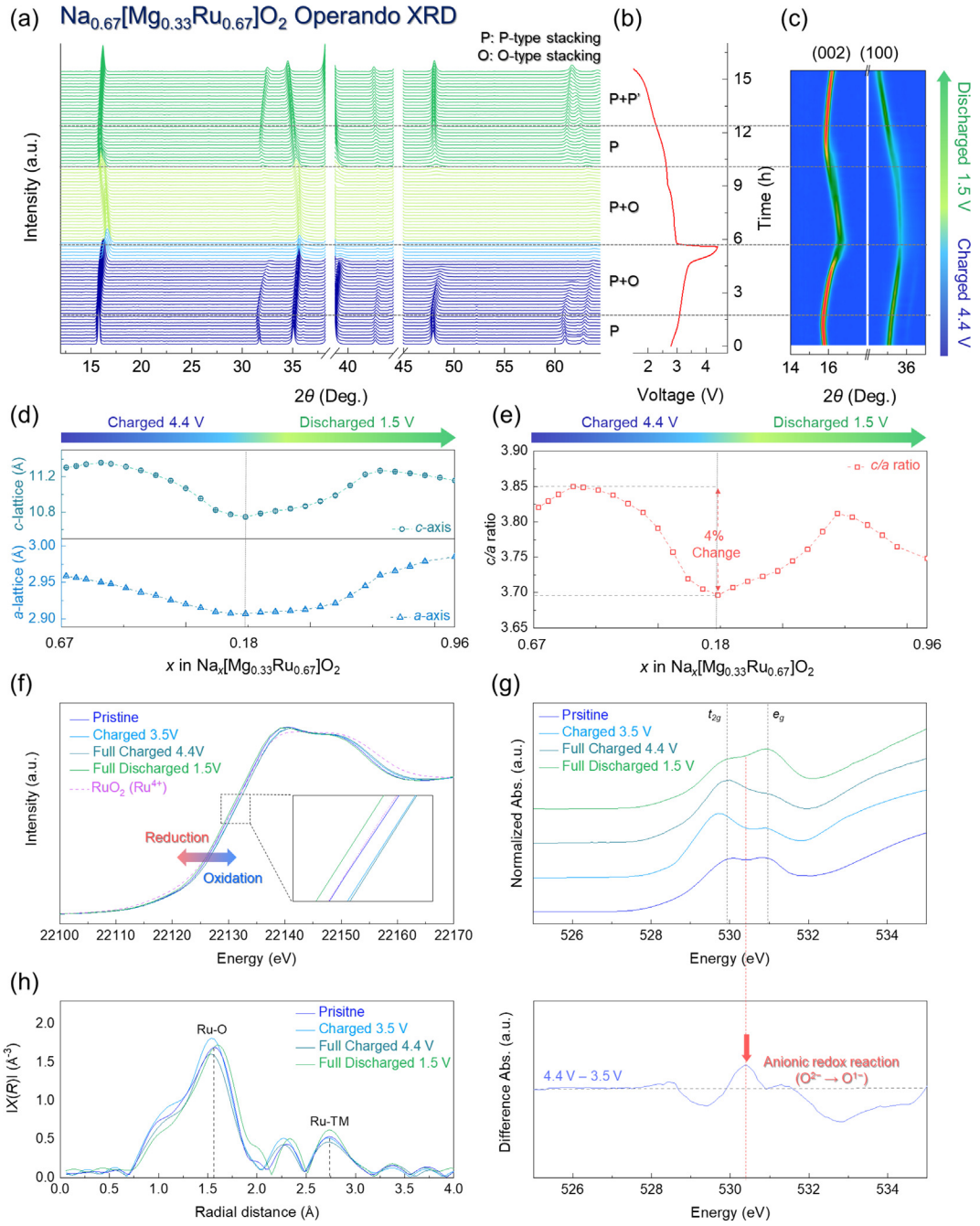

Fig. 3. (a) Operando synchrotron XRD pattern of P2-$Na_{0.67}[Mg_{0.33}Ru_{0.67}]O_2$ during charge/discharge. The 2θ angles of collected operando synchrotron XRD patterns were converted to angles corresponding to λ = 1.54178 Å (the wavelength of a conventional X-ray tube source with Cu K_α) for easy comparison with other studies. (b) Charge/discharge curves of P2-$Na_{0.67}[Mg_{0.33}Ru_{0.67}]O_2$ during operando synchrotron XRD measurement at 30 mA g^{-1} current density in the voltage range of 1.5–4.4 V. (c) Magnified view of (002) and (100) planes using results of operando XRD of P2-$Na_{0.67}[Mg_{0.33}Ru_{0.67}]O_2$. (d) Change in *c* and *a* lattice parameter as a function of Na content in $Na_x[Mg_{0.33}Ru_{0.67}]O_2$ ($0 \le x \le 1$), verified using Rietveld refinement. (e) *c*/*a* ratio using results of (d). Ex-situ analyses of $Na_x[Mg_{0.33}Ru_{0.67}]O_2$ for (f) Ru K-edge XANES spectra, (g) O K-edge soft XAS spectra, and difference spectra (lower panel) of soft XAS results. (h) Ru K-edge EXAFS spectra.

Na^+ de/intercalation that contributed to the advanced cycle stability [35]. These small changes of the lattice parameters cause the active particles to maintain their original crystal structure and morphology even after 100 cycles (Fig. S5).

3.3. Redox reaction in P2-$Na_{0.67}[Mg_{0.33}Ru_{0.67}]O_2$ during Na^+ de/intercalation

To investigate the redox reactions in P2-NMRO during Na^+ de/intercalation, we performed the ex-situ XAS analyses. As presented in Fig. 3(f), it was verified that the Ru K-edge X-ray absorption near-edge structure (XANES) spectra shifted toward higher energy level on charging to 3.5 V, which indicate the oxidation of Ru cation during Na^+ deintercalation from $Na_{0.67}[Mg_{0.33}Ru_{0.67}]O_2$ to $Na_{0.25}[Mg_{0.33}Ru_{0.67}]O_2$. During further charging to 4.4 V, however, there was no significant shift of Ru K-edge toward high energy level, even though ~0.25 mol Na^+ are deintercalated from $Na_{0.25}[Mg_{0.33}Ru_{0.67}]O_2$. Assuming that all of the deintercalated Na^+ ions charged to 3.5 V are charge compensated by the oxidation of Ru^{4+}, the oxidation state of Ru would be close to 4.6+, which also indicates that the other oxidation reaction, which is likely to be the anionic redox reaction of O^{2-}/O^-, has occurred during charging

from 3.5 to 4.4 V before the full oxidation of all Ru cations from 4+ to 5+. During discharge, the Ru K-edge was shifted to lower energy level than the pristine state, caused by the additional Na^+ intercalation into $Na_{0.67}[Mg_{0.33}Ru_{0.67}]O_2$. To confirm occurrence of anionic redox reaction of O^{2-}/O^- in P2-NMRO during charge/discharge, we performed the ex-situ O K-edge soft XAS analyses (Fig. 3g). During charging to 4.4 V, the rise of the threshold region (530.5 eV) between unoccupied Ru 4*d*-O 2*p* t_{2g} and e_g hybridized orbitals was observed. This result proves that an anionic O^{2-}/O^{1-} redox reaction occurred in P2-NMRO without full oxidation from Ru^{4+} to Ru^{5+}, as confirmed by the difference plot of soft XAS results (red arrow in Fig. 3g) [28,36–38]. And the difference of the pristine and the 1.5 V-discharged samples in the O K-edge results is attributed to their difference of oxidation states of Ru cation. Pre-edge region of O K-edge consists of Ru 4*d*-O 2*p* t_{2g} and e_g due to hybridization of Ru and O. Therefore, it is greatly affected not only by anionic redox of O but also by cationic redox of Ru. It was verified that P2-NMRO has the additionally intercalated 0.3 mol Na^+ in the structure after discharging to 1.5 V, compared to the pristine state (Fig. 3d). Ex-situ Ru-K-edge XANES analyses (Fig. 3f) show that Ru^{4+}/Ru^{3+} reduction occurred during discharging to 1.5 V, which resulted in difference of the O K-edge sXAS between the pristine and the 1.5 V-discharged states. In addition, the Ru K-edge extended X-ray absorption fine structure (EXAFS) analyses revealed the reversible change of the local structural environments in RuO_6 octahedra bond, which is attributed to the reversible cationic (Ru^{4+}/Ru^{5+}) and anionic (O^{2-}/O^{1-}) redox reactions during Na^+ de/intercalation (Fig. 3h). Ru–O distance is decreased upon charging to 3.5 V, resulting from the oxidation of Ru^{4+}/Ru^{5+}. During further charging to 4.4 V, Ru–O peak shows the significant variation caused by anionic redox reactions that result in the distortion of RuO_6 local environment. After fully discharging to 1.5 V, the Ru–O distance is further increased due to the partial reduction of Ru^{4+}/Ru^{3+} compared to the pristine state. These observations are consistent with the previously reported results on other cathode materials that experienced both cationic and anionic redox reactions [15,39,40].

We also performed ex-situ XPS analysis to investigate the redox reaction mechanism of P2-NMRO. The Ru 3*d* spectrum of the pristine state was composed of a simple spin-orbit doublet with $3d_{5/2}$ (~282.2 eV) and $3d_{3/2}$ (~284.6 eV), and energetically overlapped with the C 1*s* spectrum (Fig. S6) [41]. To enhance the accuracy of peak deconvolution, additional satellite structure peaks were refined, as previously reported [42]. The shift of Ru $3d_{5/2}$ peaks of P2-NMRO toward higher energy level upon charging to 3.5 V indicates the oxidation of Ru^{4+}/Ru^{5+}. During further desodiation to full charge (4.4 V), on the other hand, there was negligible shift of Ru $3d_{5/2}$, which indicates that further oxidation of Ru cation negligibly occurred during charging from 3.5 to 4.4 V. These results are consistent with the changes observed in the Ru K-edge as shown in ex-situ XANES analysis. Moreover, the O 1*s* spectrum of P2-NMRO (Fig. S7) revealed that the oxidized oxygen species peak (peroxo-like lattice oxygen of O_2^{n-}, ~531.5 eV, red peak in Fig. S7) was increased/decreased during charge/discharge after the 3.5 V-charged state, which implies the occurrence of the oxygen redox reaction in P2-NMRO [41,43].

The redox mechanism of P2-NMRO during Na^+ de/intercalation was investigated using first-principles calculation. Fig. 4(a) presents the projected density of states (pDOS) of Ru 4*d* and O 2*p* orbitals of $Na_x[Mg_{0.33}Ru_{0.67}]O_2$ with various Na contents

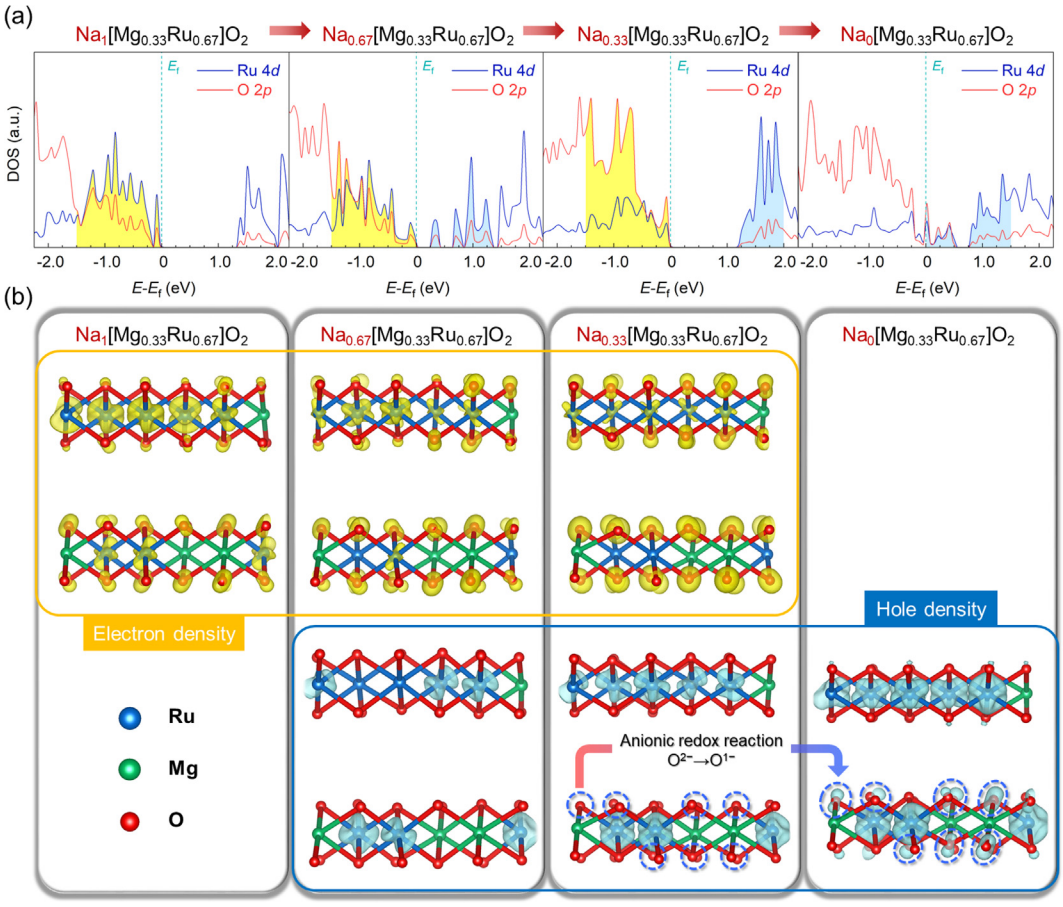

Fig. 4. (a) pDOS of Ru 4*d* and O 2*p* of $Na_x[Mg_{0.33}Ru_{0.67}]O_2$ ($0 \le x \le 1$). (b) Visualized pDOS on O 2*p* and Ru 4*d* orbitals of $Na_x[Mg_{0.33}Ru_{0.67}]O_2$ ($0 \le x \le 1$), electron density (yellow) and hole density (blue). (For interpretation of the references to colour in this figure legend, the reader is referred to the web version of this article.)

($0 \leq x \leq 1$). For x = 1 and 0.67, the electron density of the Ru 4*d* orbital nearby the Fermi level was larger than that of the O 2*p* orbital, indicating that the Na^+ extraction in the structure is dominated by Ru-based cationic redox reaction. At x = 0.33, the pDOS of the O 2*p* orbital on $Na_{0.33}[Mg_{0.33}Ru_{0.67}]O_2$ is strengthened nearby the Fermi level compared with that of the Ru 4*d* orbital. This result indicates that the O^{2-}/O^{1-} anionic redox reaction becomes activated during further Na^+ extraction from $Na_{0.33}[Mg_{0.33}Ru_{0.67}]O_2$, which can also be observed from the hole densities of the neighboring Fermi level at pDOS of the O 2*p* orbital for the $Na_0[Mg_{0.33}Ru_{0.67}]O_2$ (x = 0) composition. The pDOS data support the experimental results from XAS and XPS, which demonstrates the energetic availability of anionic oxidation at the later part of charging.

Charge densities near the Fermi level for each composition were visualized using the pDOS data on Ru 4*d* and O 2*p* orbitals to investigate the redox behavior of P2-NMRO at the atomic scale (Fig. 4b). At the early stage of desodiation, gradual shrinkage of the occupied Ru 4*d* orbital was observed from cationic oxidation. Anionic redox appeared after $Na_{0.33}[Mg_{0.33}Ru_{0.67}]O_2$, where the hole density of oxygen started to increase. We also calculated the integrated spin moment to verify the overall redox reactions of Ru and O ions in $Na_x[Mg_{0.33}Ru_{0.67}]O_2$ during Na^+ de/intercalation, and it was demonstrated through comparison with various compositions. As

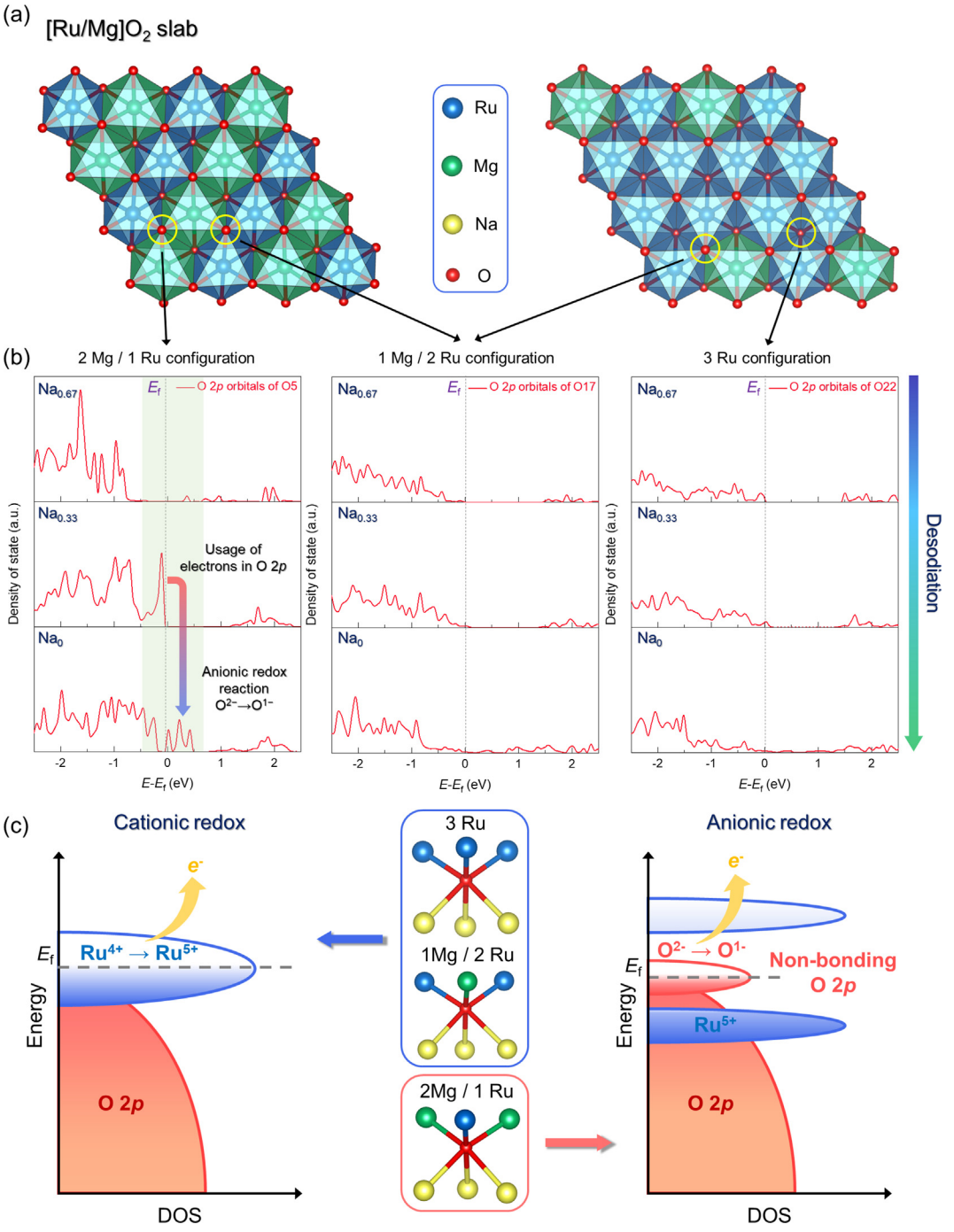

Fig. 5. (a) Magnified view of crystal structure corresponding to the *ab* plane of P2-$Na_{0.67}[Mg_{0.33}Ru_{0.67}]O_2$. (b) pDOS of O 2*p* orbitals along various local configurations in $Na_x[Mg_{0.33}Ru_{0.67}]O_2$ (x = 0.67, 0.33, and 0). (c) Illustration showing molecular orbitals that determine cationic and anionic redox reactions based on various local configurations.

shown in Fig. S8, whereas the total magnetic moment of Ru ions changed during Na^+ extraction from $Na_1[Mg_{0.33}Ru_{0.67}]O_2$ to $Na_{0.33}[Mg_{0.33}Ru_{0.67}]O_2$, it did not change after further Na^+ extraction from $Na_{0.33}[Mg_{0.33}Ru_{0.67}]O_2$. Instead the total magnetic moment of O ions increased during Na^+ extraction from $Na_{0.33}[Mg_{0.33}Ru_{0.67}]O_2$ to $Na_0[Mg_{0.33}Ru_{0.67}]O_2$. These results indicate that anionic redox (O^{2-}/O^{1-}) can occur at $Na_{0.33}[Mg_{0.33}Ru_{0.67}]O_2$ after cationic redox (Ru^{4+}/Ru^{5+}) reactions. In addition, the theoretical redox mechanism of P2-NMRO was confirmed through Bader charge analyses. Fig. S9 presents the change of the net effective charges on Ru and O ions with various Na contents in $Na_x[Mg_{0.33}Ru_{0.67}]O_2$, which also implies the occurrence of an anionic redox reaction after Na^+ extraction at $Na_{0.33}[Mg_{0.33}Ru_{0.67}]O_2$.

3.4. Origin of anionic redox reactions in P2-$Na_{0.67}[Mg_{0.33}Ru_{0.67}]O_2$

The aforementioned electrochemical and computational data demonstrate that both cationic and anionic redox reactions are employed during charge/discharge of P2-NMRO. However, one may wonder why anionic redox is activated before the sufficient oxidation of Ru cation to +5. The origin of the anionic redox is elucidated through the calculation of pDOS for individual atoms in P2-$Na_x[Mg_{0.33}Ru_{0.67}]O_2$ with various Na contents ($0 \leq x \leq 0.67$).

As shown in Fig. 5(a), various local environments can be created depending on the combination of Ru and Mg around oxygen ions. In the P2-type structure, randomly distributed Ru and Mg in the metal layer enable three configurations: (1) one Ru/two Mg, (2) two Ru/one Mg, and (3) three Ru. According to our result, the availability of oxygen redox is strongly dependent on the local cation environment around the oxygen. When the oxygen is surrounded by two or more Ru atoms (case 2, 3), a general cationic redox reaction appears as O 2*p* orbitals are not dominant near the Fermi level. However, within the local configuration of 1 Ru and 2 Mg, the generation of oxygen orbitals near the Fermi level is observed at $Na_{0.33}[Mg_{0.33}Ru_{0.67}]O_2$ (Fig. 5b). It indicates that the anionic redox reaction becomes more active as the redoxable Mg–O–Na bonds are generated within the low sodium contents in the structure. The linear bond creates a non-bonding O 2*p* state with a large energy difference between Mg/Na 3*s* and O 2*p*. Because labile oxygen electrons can be used for redox reactions, forming the Mg–O–Na local environment that enhances the activity of the anionic redox from the early state of charge even before the full oxidation of Ru [44,45]. Although non-bonding O 2*p* states have been usually generated in Li-rich or Na-rich oxide compounds [29,46], the energetic favorability of Mg in the transition-metal layer induces a specific Mg–O–Na local environment that activates the anionic redox in the Na-deficient NMRO composition.

Identical results were obtained through Bader charge analysis. As shown in the details of the Bader charge analyses (Tables S3 and S4), it was confirmed that the effective charge in oxygen ions surrounded by one Ru and two Mg was dramatically decreased compared with the other cases. The critical role of the oxygen local environment is illustrated in the schematic diagram in Fig. 5(c). Unlike other known Ru-based layered oxide cathode materials with oxygen redox reaction, most of Na^+ in the P2-NMRO structure with 1:1 molar ratio of Na and Ru should be deintercalated during the oxidation from Ru^{4+} to Ru^{5+}. At that time, when Mg is abundant around oxygen ions in the structure after deintercalation of considerable Na contents, the energy level of oxygen will increase and it can trigger the oxidation of oxygen ions during Na^+ deintercalation from the $Na_x[Mg_{0.33}Ru_{0.67}]O_2$ structure. Therefore, anionic redox reaction of O^{2-}/O^- can occur in P2-NMRO before the full oxidation of all Ru^{4+} cations to Ru^{5+}. Moreover, we compared the available capacities among P2-NMRO and other Ru-based layered-oxide cathodes for NIBs. As tabulated in Table 1 [13,15,47–51], it was confirmed that P2-NMRO has large specific capacity and electrochemical stability even at high charge cut-off voltage of 4.4 V (vs. Na^+/Na). These results indicate that the control of the oxygen local environment provides a strategy to improve the energy density of NIB cathode materials by enabling the anionic redox reaction.

Table 1
Comparing the available capacities among P2-$Na_{0.67}[Mg_{0.33}Ru_{0.67}]O_2$ and other Ru-based layered-oxide cathodes for Na-ion batteries.

Ru-based layered-oxide cathode	Voltage range (V vs. Na^+/Na)	Dischargecapacity (mA h g^{-1})	Reference
P2-$Na_{0.67}[Mg_{0.33}Ru_{0.67}]O_2$	1.5–4.4	172	This work
P2-$Na_{0.66}Li_{0.22}Ru_{0.78}O_2$	1.5–4.5	158	[15]
O3-$Na_{0.6}Li_{0.35}Fe_{0.1}Ru_{0.55}O_2$	1.5–4.0	148	[47]
O3-$NaMg_{0.5}Ru_{0.5}O_2$	1.5–4.0	86	[48]
Na_2RuO_3	1.5–4.0	147	[49]
$Na_{1.33}Fe_{0.33}Ru_{0.33}O_2$	1.5–4.0	120	[50]
$Na_2Sn_{0.25}Ru_{0.75}O_3$	1.5–4.2	140	[51]
Na_3RuO_4	1.5–4.0	128	[13]

4. Conclusions

In this work, we demonstrated that both cationic and anionic redox reactions occur in P2-NMRO, which was enabled by modulating the local environment of oxygen ions. From the combined experimental and computational analyses on the redox mechanism, anionic redox was observed before the full oxidation of all Ru^{4+} cations to Ru^{5+}. It was revealed that the Mg-rich oxygen local environment facilitates the formation of Mg–O–Na bonds, generating reversibly redoxable non-bonding O 2*p* states from the early state of charge. Using cationic and anionic redox reactions, P2-NMRO delivered a specific capacity of ~172 mA h g^{-1} while exhibiting excellent power-capability and structural and electrochemical stability, which was attributed to the continuous P2-OP4 phase transition. We believe that our finding provides an effective strategy for the design of a high-energy-density NIB cathode with anionic redox and structural stability through the control of the local configurations and electronic structure.

Declaration of competing interest

The authors declare the following financial interests/personal relationships which may be considered as potential competing interests: [Jongsoon Kim reports financial support was provided by National Research Foundation of Korea, Korea Institute of Material Science and Korea Institute of Science and Technology Information. Kyojin Ku reports financial support was provided by National Research Foundation of Korea.]

Acknowledgments

This work was supported by the National Research Foundation of Korea (NRF) grant funded by the Korean government (MSIT) (2021R1A2C1014280). This work was also supported by the "Regional Innovation Strategy (RIS)" through the National Research Foundation of Korea (NRF) funded by the Ministry of Education (MOE) (2021RIS-004) and the Fundamental Research Program of the Korea Institute of Material Science (KIMS) (PNK9370). In addition, the calculation resources were supported by the Supercomputing Center in Korea Institute of Science and Technology Information (KISTI) (KSC-2022-CRE-0030).

Appendix A. Supplementary material

Supplementary data to this article can be found online at https://doi.org/10.1016/j.jechem.2023.05.016.

References

[1] J.B. Goodenough, Energy Environ. Sci. 7 (2014) 14–18.
[2] M. Aneke, M. Wang, Appl. Energy 179 (2016) 350–377.
[3] S.J. Davis, N.S. Lewis, M. Shaner, S. Aggarwal, D. Arent, I.L. Azevedo, S.M. Benson, T. Bradley, J. Brouwer, Y.M. Chiang, C.T.M. Clack, A. Cohen, S. Doig, J. Edmonds, P. Fennell, C.B. Field, B. Hannegan, B.M. Hodge, M.I. Hoffert, E. Ingersoll, P. Jaramillo, K.S. Lackner, K.J. Mach, M. Mastrandrea, J. Ogden, P.F. Peterson, D.L. Sanchez, D. Sperling, J. Stagner, J.E. Trancik, C.J. Yang, K. Caldeira, Science 360 (2018) eaas9793.
[4] B. Dunn, H. Kamath, J.M. Tarascon, Science 334 (2011) 928–935.
[5] D. Larcher, J.M. Tarascon, Nat. Chem. 7 (2015) 19–29.
[6] J. Wang, Y. Wang, D.H. Seo, T. Shi, S. Chen, Y. Tian, H. Kim, G. Ceder, Adv. Energy Mater. 10 (2020) 1903968.
[7] X. Judez, G.G. Eshetu, C. Li, L.M. Rodriguez-Martinez, H. Zhang, M. Armand, Joule 2 (2018) 2208–2224.
[8] H. Kim, H. Kim, Z. Ding, M.H. Lee, K. Lim, G. Yoon, K. Kang, Adv. Energy Mater. 6 (2016) 1–38.
[9] J. Kim, I. Park, H. Kim, K.Y. Park, Y.U. Park, K. Kang, Adv. Energy Mater. 6 (2016) 6–9.
[10] W. Ko, M.K. Cho, J. Kang, H. Park, J. Ahn, Y. Lee, S. Lee, S. Lee, K. Heo, J. Hong, J.K. Yoo, J. Kim, Energy Storage Mater. 46 (2022) 289–299.
[11] J. Kang, J. Ahn, H. Park, W. Ko, Y. Lee, S. Lee, S. Lee, S.K. Jung, J. Kim, Adv. Funct. Mater. 32 (2022) 2201816.
[12] K. Sato, M. Nakayama, A.M. Glushenkov, T. Mukai, Y. Hashimoto, K. Yamanaka, M. Yoshimura, T. Ohta, N. Yabuuchi, Chem. Mater. 29 (2017) 5043–5047.
[13] Y. Qiao, S. Guo, K. Zhu, P. Liu, X. Li, K. Jiang, C.-J. Sun, M. Chen, H. Zhou, Energy Environ. Sci. 11 (2018) 299–305.
[14] M.M. Rahman, F. Lin, Matter 4 (2021) 490–527.
[15] X. Cao, H. Li, Y. Qiao, X. Li, M. Jia, J. Cabana, H. Zhou, Adv. Energy Mater. 10 (2020) 1903785.
[16] U. Maitra, R.A. House, J.W. Somerville, N. Tapia-Ruiz, J.G. Lozano, N. Guerrini, R. Hao, K. Luo, L. Jin, M.A. Pérez-Osorio, F. Massel, D.M. Pickup, S. Ramos, X. Lu, D. E. McNally, A.V. Chadwick, F. Giustino, T. Schmitt, L.C. Duda, M.R. Roberts, P.G. Bruce, Nat. Chem. 10 (2018) 288–295.
[17] A. Konarov, J.H. Jo, J.U. Choi, Z. Bakenov, H. Yashiro, J. Kim, S.T. Myung, Nano Energy 59 (2019) 197–206.
[18] Y. Yu, P. Karayaylali, D. Sokaras, L. Giordano, R. Kou, C.J. Sun, F. Maglia, R. Jung, F.S. Gittleson, Y. Shao-Horn, Energy Environ. Sci. 14 (2021) 2322–2334.
[19] M. Sathiya, K. Ramesha, G. Rousse, D. Foix, D. Gonbeau, A.S. Prakash, M.L. Doublet, K. Hemalatha, J.M. Tarascon, Chem. Mater. 25 (2013) 1121–1131.
[20] J. Hong, W.E. Gent, P. Xiao, K. Lim, D.H. Seo, J. Wu, P.M. Csernica, C.J. Takacs, D. Nordlund, C.J. Sun, K.H. Stone, D. Passarello, W. Yang, D. Prendergast, G. Ceder, M.F. Toney, W.C. Chueh, Nat. Mater. 18 (2019) 256–265.
[21] M. Saubanère, E. McCalla, J.M. Tarascon, M.L. Doublet, Energy Environ. Sci. 9 (2016) 984–991.
[22] J. Rodríguez-Carvajal, Comm. Powder Diffr. (IUCr). Newsl. 26 (2001) 12–19.
[23] B. Ravel, M. Newville, Phys. Scr. T T 115 (2005) 1007–1010.
[24] G. Kresse, J. Furthmüller, Comput. Mater. Sci. 6 (1996) 15–50.
[25] P.E. Blöchl, Phys. Rev. B 50 (1994) 17953–17979.
[26] J.P. Perdew, K. Burke, M. Ernzerhof, Phys. Rev. Lett. 77 (1996) 3865–3868.
[27] V.I. Anisimov, F. Aryasetiawan, A.I. Lichtenstein, J. Phys. Condens. Matter 9 (1997) 767–808.
[28] J. Ahn, J. Kang, M. Kyung Cho, H. Park, W. Ko, Y. Lee, H.S. Kim, Y.H. Jung, T.Y. Jeon, H. Kim, W.H. Ryu, J. Hong, J. Kim, Adv. Energy Mater. 11 (2021) 2102311.
[29] D.H. Seo, J. Lee, A. Urban, R. Malik, S. Kang, G. Ceder, Nat. Chem. 8 (2016) 692–697.
[30] A. Van der Ven, J.C. Thomas, Q. Xu, J. Bhattacharya, Math. Comput. Simul. 80 (2010) 1393–1410.
[31] G. Henkelman, B.P. Uberuaga, H. Jónsson, J. Chem. Phys. 113 (2000) 9901–9904.
[32] K. Momma, F. Izumi, J. Appl. Crystallogr. 44 (2011) 1272–1276.
[33] H. Liu, X. Gao, J. Chen, J. Gao, S. Yin, S. Zhang, L. Yang, S. Fang, Y. Mei, X. Xiao, L. Chen, W. Deng, F. Li, G. Zou, H. Hou, X. Ji, J. Power Sources 508 (2021).
[34] D. Pahari, S. Puravankara, J. Power Sources 455 (2020).
[35] M. Jeong, W. Lee, S. Yun, W. Choi, H. Park, E. Lee, J. Kim, S.J. Cho, N.H. Lee, H.J. Shin, W.S. Yoon, Adv. Energy Mater. 12 (2022) 2103052.
[36] S. Myeong, W. Cho, W. Jin, J. Hwang, M. Yoon, Y. Yoo, G. Nam, H. Jang, J.G. Han, N.S. Choi, M.G. Kim, J. Cho, Nat. Commun. 9 (2018) 3285.
[37] R.A. House, L. Jin, U. Maitra, K. Tsuruta, J.W. Somerville, D.P. Förstermann, F. Massel, L. Duda, M.R. Roberts, P.G. Bruce, Energy Environ. Sci. 11 (2018) 926–932.
[38] C. Cheng, M. Ding, T. Yan, K. Dai, J. Mao, N. Zhang, L. Zhang, J. Guo, Energies 13 (2020) 5729.
[39] G. Assat, A. Iadecola, C. Delacourt, R. Dedryvère, J.M. Tarascon, Chem. Mater. 29 (2017) 9714–9724.
[40] M. Otoyama, Q. Jacquet, A. Iadecola, M. Saubanère, G. Rousse, J. Tarascon, Adv. Energy Mater. 9 (2019) 1803674.
[41] D. Foix, M. Sathiya, E. McCalla, J.M. Tarascon, D. Gonbeau, J. Phys. Chem. C 120 (2016) 862–874.
[42] D. Cabrera-German, G. Gomez-Sosa, A. Herrera-Gomez, Surf. Interface Anal. 48 (2016) 252–256.
[43] A.J. Naylor, E. Makkos, J. Maibach, N. Guerrini, A. Sobkowiak, E. Björklund, J.G. Lozano, A.S. Menon, R. Younesi, M.R. Roberts, K. Edström, M.S. Islam, P.G. Bruce, J. Mater. Chem. A 7 (2019) 25355–25368.
[44] A. Konarov, H.J. Kim, J. Jo, N. Voronina, Y. Lee, Z. Bakenov, J. Kim, S. Myung 10 (2020) 2001111.
[45] M. Okubo, A. Yamada, ACS Appl. Mater. Interfaces 9 (2017) 36463–36472.
[46] B. Mortemard De Boisse, G. Liu, J. Ma, S.I. Nishimura, S.C. Chung, H. Kiuchi, Y. Harada, J. Kikkawa, Y. Kobayashi, M. Okubo, A. Yamada, Nat. Commun. 7 (2016) 1–9.
[47] M. Jia, Y. Qiao, X. Li, F. Qiu, X. Cao, P. He, H. Zhou, ACS Appl. Mater. Interfaces 12 (2020) 851–857.
[48] M. Jia, Y. Qiao, X. Li, K. Jiang, H. Zhou, J. Mater. Chem. A 7 (2019) 20405–20413.
[49] M. Tamaru, X. Wang, M. Okubo, A. Yamada, Electrochem. Commun. 33 (2013) 23–26.
[50] J. Xu, Z. Han, K. Jiang, P. Bai, Y. Liang, X. Zhang, P. Wang, S. Guo, H. Zhou, Small 16 (2020) 1904388.
[51] P. Rozier, M. Sathiya, A.-R. Paulraj, D. Foix, T. Desaunay, P.-L. Taberna, P. Simon, J.-M. Tarascon, Electrochem. Commun. 53 (2015) 29–32.